

**Fig. 3.** Quantitative analysis of crystal growth. (A) Filtering: Areas affected by other impurities (with a diameter  $\sigma_p$ ) are not taken into account by excluding the shaded area for analysis. (B) Crystal growth profiles of shells around  $I_{10}$ ; 0 to 5  $\mu\text{m}$  (crosses), 5 to 10  $\mu\text{m}$  (squares), 10 to 15  $\mu\text{m}$  (circles), and 15 to 20  $\mu\text{m}$  (plus signs). (C) Crystal growth profile of the 15- to 20- $\mu\text{m}$  shell for  $I_5$  (squares, inset only),  $I_{10}$  (circles),  $I_{13}$  (diamonds), and  $I_{20}$  (triangles). (Inset) Frustration of crystal growth increases both as the impurity is approached and as  $\alpha$  is decreased.  $r_C$  close to  $I_5$  is  $\sim 0$ , because no local increase of order occurs during the recorded image sequence. Rates at 0.5, 1.5, and 2.5  $\sigma_p$  are based on shells of  $\sigma_p$  thickness. Other  $r_C$  values are obtained from shells 5  $\mu\text{m}$  thick;  $r_C$  at 5  $\sigma_p$  corresponds to the 5- to 10- $\mu\text{m}$  shell.

(during linear rise) as  $r_C = \Delta\langle |\dot{\psi}_6| \rangle / \Delta t$ . The effect of an impurity's size on the local growth rate can now be compared quantitatively (Fig. 3C, inset). Several general trends can be observed. First, a larger  $\alpha$  results in a higher rate close to the impurity. Second, the rate rises faster per shell as  $\alpha$  increases. Finally, the rates for different  $\alpha$  apparently approach a different maximum rate at less than  $\sim 17$  particle

diameters instead of converging to a bulk growth rate of  $\sim 0.02 \text{ min}^{-1}$  [measured at 5 to 25  $\mu\text{m}$  above the sample bottom in the control sample (fig. S2) and at sample locations far ( $>40 \mu\text{m}$ ) from impurities]. Relatively far from the impurity ( $>8 \sigma_p$ ), a trend is observed between the growth rate and  $\alpha$ . We argue that grain boundaries are pinned by impurities (Fig. 2, A and B): If nearby impurities are present, more boundaries appear. To approximate the ideal case of no nearby impurities, the image is filtered (Fig. 3A); grain boundaries leading to impurities further away are not included. The obtained increase of  $r_C$  by a factor of 1.6 for the filtered  $I_{21}$  sequence therefore is too high, whereas not filtering leads to values that are too low. We therefore expect the rates to converge at sufficient distance, which might very well be beyond  $\sim 17$  particle diameters. Furthermore, the growth rate in the first layer is about zero for all  $\alpha$ —a confirmation of the observed fluid layer (Fig. 2D).

Using laser confocal scanning microscopy, we have shown that the bulk crystal growth rate is substantially reduced near impurities. The extent to which the growth rate is reduced decreases with distance to the impurity. The size ratio  $\alpha$  is a critical factor; the (local) curvature of an impurity is therefore crucial for real hard-sphere-like systems such as metals. Grain boundaries are pinned by the impurities, and the first particle layer around the impurity remains fluid. Impurities locally substantially frustrate the crystal growth and structure of hard-sphere systems, the very same impurities that, in a different scenario, can induce heterogeneous crystal nucleation (3).

## References and Notes

- N. Kubota, *Cryst. Res. Technol.* **36**, 749 (2001).
- T. A. Land, T. L. Martin, S. Potapenko, G. T. Palmore, J. J. De Yoreo, *Nature* **399**, 442 (1999).
- A. Cacciuto, S. Auer, D. Frenkel, *Nature* **428**, 404 (2004).
- T. A. Eremina et al., *J. Cryst. Growth* **273**, 586 (2005).
- M. Rak et al., *J. Cryst. Growth* **273**, 577 (2005).
- A. J. Malkin, Y. G. Kuznetsov, T. A. Land, J. J. Deyoreo, A. McPherson, *Nat. Struct. Biol.* **2**, 956 (1995).
- K. J. Davis, P. M. Dove, J. J. De Yoreo, *Science* **290**, 1134 (2000).
- D. T. J. Hurler, P. Rudolph, *J. Cryst. Growth* **264**, 550 (2004).
- R. Kern, R. Dassonville, *J. Cryst. Growth* **116**, 191 (1992).
- S. D. Durbin, G. Feher, *Annu. Rev. Phys. Chem.* **47**, 171 (1996).
- D. Nelson, M. Rubinstein, F. Spaepen, *Philos. Mag. A* **46**, 105 (1982).
- S. Auer, D. Frenkel, *Nature* **413**, 711 (2001).
- M. Dijkstra, *Phys. Rev. Lett.* **93**, 103303 (2004).
- S. Auer, D. Frenkel, *Phys. Rev. Lett.* **91**, 015703 (2003).
- G. Bosma et al., *J. Colloid Interface Sci.* **245**, 292 (2002).
- E. H. A. de Hoog, thesis, University of Utrecht, Utrecht, the Netherlands (2001).
- P. Schall, I. Cohen, D. A. Weitz, F. Spaepen, *Science* **305**, 1944 (2004).
- D. Nelson, *Defects and Geometry in Condensed Matter Physics* (Cambridge Univ. Press, Cambridge, 2002), pp. 68–91.
- J. C. Crocker, D. G. Grier, *J. Colloid Interface Sci.* **179**, 298 (1996).
- G. Bosma is acknowledged for particle synthesis. This work is part of the research program of the Stichting voor Fundamenteel Onderzoek der Materie (FOM), which is financially supported by the Nederlandse Organisatie voor Wetenschappelijk Onderzoek (NWO). Support through the Transregio Sonderforschungsbereich 6 (SFB-TR6) through the Deutsche Forschungsgemeinschaft (DFG) is acknowledged.

## Supporting Online Material

www.sciencemag.org/cgi/content/full/309/5738/1231/DC1  
SOM Text  
Figs. S1 to S3

5 April 2005; accepted 20 July 2005  
10.1126/science.1113207

# Osmium Isotope Evidence for an s-Process Carrier in Primitive Chondrites

A. D. Brandon,<sup>1\*</sup> M. Humayun,<sup>2†</sup> I. S. Puchtel,<sup>3</sup> I. Leya,<sup>4</sup> M. Zolensky<sup>5</sup>

Osmium extracted from unequilibrated bulk chondrites has isotope anomalies consistent with an insoluble s-process carrier, termed Os(i) here. Osmium from metamorphosed bulk chondrites does not have isotope anomalies, implying that the Os(i) carrier was destroyed by metamorphism. The isotopic homogeneity of metamorphosed bulk chondrites is consistent with extremely effective mixing of presolar grains from varied sources in the nebula. Osmium in the Os(i) carrier is likely from nucleosynthetic sites with a neutron density about two to four times as high as that of the average solar s-process Os.

Presolar grains (such as SiC and nanodiamonds) are prevalent in unequilibrated chondrites and preserve material from nucleosynthetic processes occurring in the stars from which these grains formed (1, 2). The degree to which these grains and solar material were mixed in the solar nebula is uncertain but important for discerning solar system pro-

cesses. Isotopic anomalies have been identified in presolar grains and Ca-Al-rich inclusions (CAIs) in chondrites (1–4). We measured Os isotopes to assess heterogeneities in bulk chondrite meteorites:  $^{184}\text{Os}$  is produced by the p process only;  $^{186}\text{Os}$  [p-process contribution 1.1% relative (5)] and  $^{187}\text{Os}$  are produced by the s process and radiogenic decay from

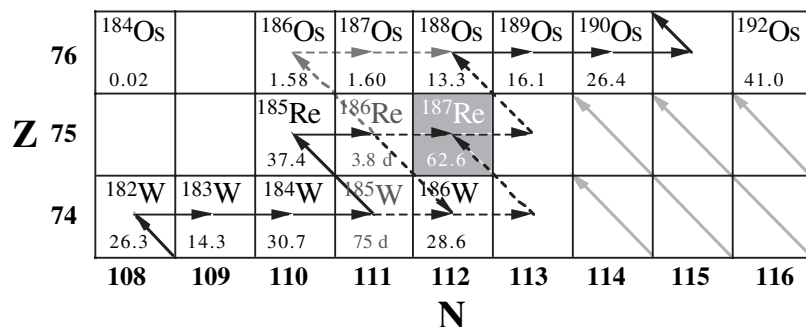


**Fig. 1.** The *s*-process pathway in the W-Os region. Stable isotopes are indicated in black letters with their isotopic abundances given below the nuclide symbol. Long-lived radioactive elements are indicated in gray letters with their half-lives shown below the nuclide symbol; radionuclides that are not part of this discussion are left blank. The *s*-process pathway comes through monoisotopic  $^{181}\text{Ta}$ , branches first at  $^{185}\text{W}$ , and then again at  $^{186}\text{Re}$ . Both branches combine at  $^{188}\text{Os}$ . Three processes occur at  $^{186}\text{Re}$ :  $\beta^-$  decay to  $^{186}\text{Os}$  (92%), electron capture to  $^{186}\text{W}$  (8%, lower at stellar temperatures), and neutron capture to  $^{187}\text{Re}$ . The *r* process is shown as oblique long arrows emerging from the lower right corner of the field and terminating at the first stable nuclide. Isotopes shielded from the *r* process include  $^{186}\text{Os}$  and  $^{187}\text{Os}$ ;  $^{184}\text{Os}$  is a *p*-only isotope;  $^{192}\text{Os}$  is an *r*-only isotope (*s*-process contribution  $\ll 1\%$  relative). Z, atomic number; N, neutron number.

$^{190}\text{Pt}$  and  $^{187}\text{Re}$ , respectively;  $^{188}\text{Os}$ ,  $^{189}\text{Os}$ ,  $^{190}\text{Os}$ , and  $^{192}\text{Os}$  are produced partly by the *s* process but are dominated by the *r*-process Pt peak (6–8) (Fig. 1). Stellar nucleosynthetic processes release their products to the interstellar medium as both gas and grains. Osmium condenses as an ultrarefractory metal alloy with Re and W, and behaves as one of the most refractory elements during condensation of stellar outflows. Ultrarefractory grains are more likely to survive nebular thermal processing. We studied seven ordinary chondrites: Chainpur LL3.4, Parnellee LL3.6, Sharps H3.4, St. Marguerite H4, Forest Vale H4, Allegan H5, and Weston H5; three enstatite chondrites: Daniels Kuil EL6, Yilmia EL6, and Indarch EH4; and three carbonaceous chondrites: Tagish Lake C2, Omans CO3, and Allende CV3. Together, these chondrites span a wide range of compositional groups and metamorphic grades.

The measured Os isotope data (9) are displayed in epsilon units (Fig. 2), where  $\epsilon_{\text{Os}}$  is  $10^4$  parts deviation from the mean of H-group ordinary chondrites measured in this study. This is because of the overlap of the H-group Os isotope ratios with those of the terrestrial materials, which are interpreted as bulk solar values (Fig. 2). The  $\epsilon_{186}$  values are corrected for  $^{190}\text{Pt}$  decay over 4.558 billion years to initial values ( $\epsilon_{186i}$ ; Fig. 2 and table S1). This

<sup>1</sup>NASA Johnson Space Center, Mail Stop KR, Houston, TX 77058, USA. <sup>2</sup>National High Magnetic Field Laboratory and Department of Geological Sciences, Florida State University, 1800 East Paul Dirac Drive, Tallahassee, FL 32310, USA. <sup>3</sup>Department of Geology, University of Maryland, College Park, MD 20742, USA. <sup>4</sup>Physikalisches Institut, Universität Bern, Sidlerstrasse 5, CH-3012 Bern, Switzerland. <sup>5</sup>NASA JSC, Mail Stop KT, Houston, TX 77058, USA.

\*To whom correspondence should be addressed. E-mail: alan.d.brandon1@jsc.nasa.gov

†These authors contributed equally to this work.

results in a systematic  $\sim 1.1$ -epsilon correction for all chondrite samples. Because  $^{189}\text{Os}$  and  $^{192}\text{Os}$  are used for correcting for instrumental mass fractionation, all data have  $\epsilon_{189}$  and  $\epsilon_{192}$  of zero. The  $^{189}\text{Os}$  and  $^{192}\text{Os}$  isotopes were chosen for normalization because in solar system Os, these isotopes contain the smallest contribution of *s*-process nucleosynthesis [4.8% and 0.4%, respectively (6–8)]. This normalization best illustrates variations in the *s*-process components relative to those in *r*-process components (10).

Tagish Lake (C2), and to a lesser extent Omans (CO3), display deficiencies in the *s*-process isotopes relative to most of the ordinary and enstatite chondrites measured, with anomalies in the order:  $^{186}\text{Os} > ^{188}\text{Os} > ^{190}\text{Os}$  (Fig. 2). These deficiencies correlate with the *s*-process abundances of each isotope. Also, Parnellee (LL3.6) and Indarch (EH4) exhibit small negative  $\epsilon_{186i}$  (98.9% *s*-process isotope) anomalies.

The variations observed in  $\epsilon_{\text{Os}}$  could result from cosmic-ray exposure effects, incomplete digestion of insoluble Os carrying phases, or inhomogeneous distribution of the *s*- and *r*-process isotopes in the solar nebula. The effects on Os isotopes from cosmic-ray exposure can be estimated (11). For an exposure age of 100 million years, the effect should be from 0.2 to 1 epsilon units for burnout and production of the different Os isotopes. The exposure age for Tagish Lake calculated from  $^{21}\text{Ne}$  is 7.8 million years (12), and hence, the effects for cosmic-ray exposure should be negligible.

Osmium is hosted in Fe-Ni alloy, refractory metal nuggets, and possibly in presolar SiC or graphite, similar to Ru (13–15). To determine whether incomplete digestion of an Os carrier was responsible for the effect, we performed a digestion of Tagish Lake using sealed metal jackets with  $\text{CO}_2$  overpressure, at temperatures

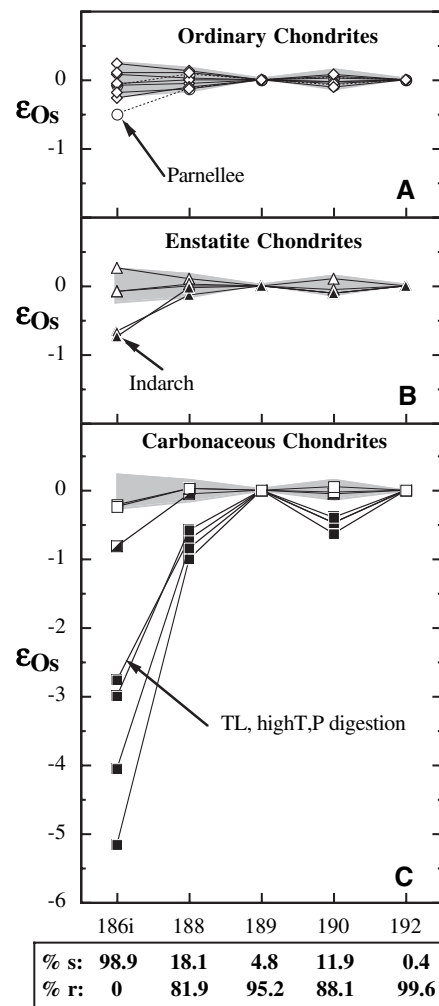
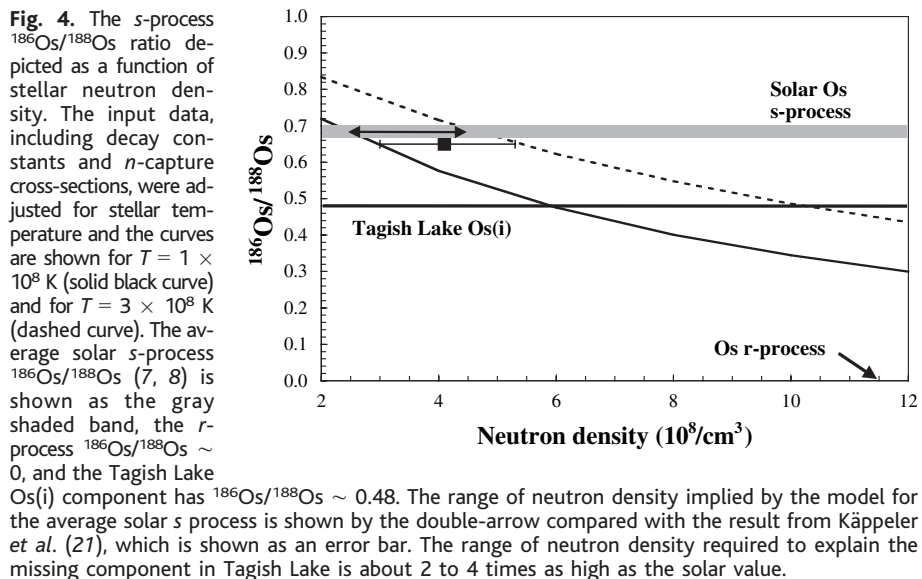
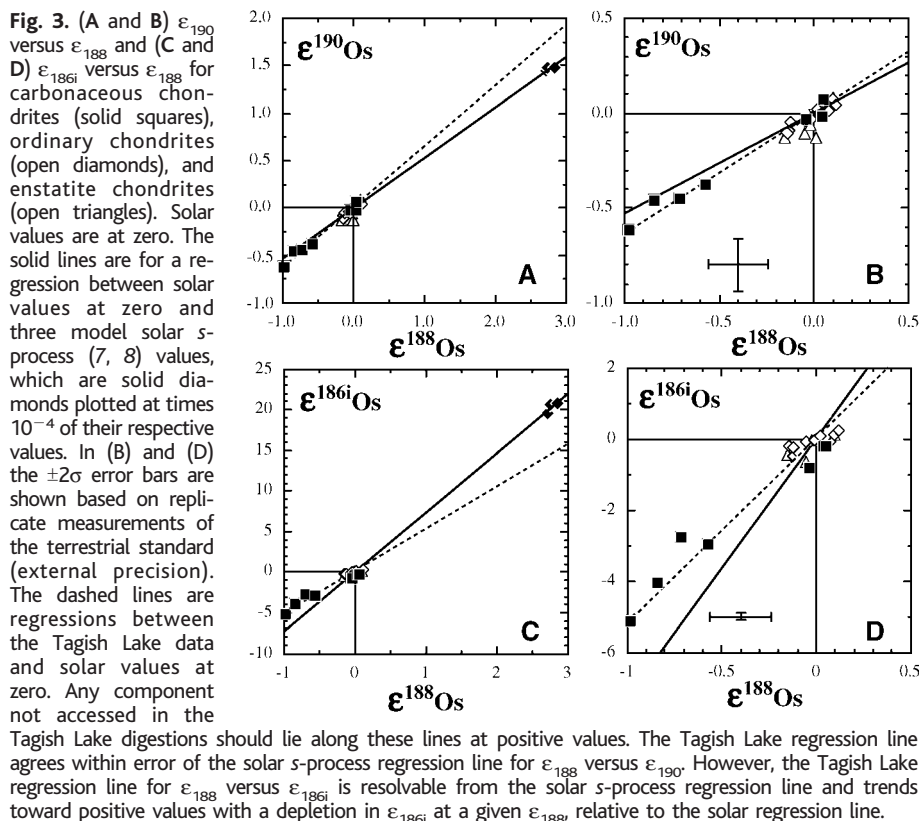


**Fig. 2.** (A) Normalized Os isotopic compositions of H-group (diamonds) and LL-group (circles) ordinary chondrites. (B) Normalized Os isotopic compositions of enstatite chondrites. Open triangles, EL6; solid triangles, Indarch EH4. (C) Normalized Os isotopic compositions of the carbonaceous chondrites Allende (open squares), Omans (half-solid squares), and Tagish Lake (TL) (solid squares). The  $^{187}\text{Os}$  data are not shown because of large variable contributions from radioactive decay (9). The shaded regions are the  $\pm 2\sigma$  error envelope on 39 runs of the terrestrial standard (external precision). Terrestrial mantle samples (table S1) all plot within these envelopes. Individual data points for each sample have  $\pm 0.25 \epsilon_{\text{Os}}$  ( $2\sigma$ ) or better uncertainties. The calculated atomic percentage of *s* and *r* processes for each isotope listed are based on models from Beer *et al.* (8).

of  $325^\circ\text{C}$  for 1 week (9, 16), compared with no overpressure,  $240^\circ$  to  $270^\circ\text{C}$ , and 48 to 72 hours for the other digestions. The Os isotopic data for this digestion retains the Os isotopic anomalies (Fig. 2) but not to the same extent as the other digestions for this rock. In addition, the four separate digestions of different clasts from the Tagish Lake meteorite show variable anomalies with systematic depletions, where  $^{186}\text{Os} > ^{188}\text{Os} > ^{190}\text{Os}$ . These observations imply that there is an *s*-process deficit in



Os extracted from Tagish Lake and suggest that whatever phase is carrying the  $s$ -process Os, it is either heterogeneously distributed or variably accessed by the digestions. From the  $s$ -process anomalies observed in Tagish Lake, it can be estimated that 30 to 50 parts per million (ppm) of the total Os (14 to 24 pg/g out of 476 ng/g) are located in the  $s$ -process carrier. If the carrier phase is presolar SiC, present at  $\sim 5$  to 8 ppm by weight of Tagish Lake (17), then the  $s$ -process Os concentration

is  $\sim 1$  to 5 ppm. The actual Os concentration could be higher because isotopically normal Os is incorporated from the stellar atmosphere. Elemental abundances in presolar SiC by synchrotron x-ray fluorescence for Ru (2 to 57 ppm) and Mo (1 to 54 ppm) (15) are of the same order of magnitude as the mean Os abundance (5 to 8 ppm, if SiC is assumed as the carrier phase) in the  $s$ -process carrier inferred here. The chemical similarity of Os to Ru indicates that some Os may occur in SiC,

even though neither element is known to form carbides. Osmium occurs as refractory metal inclusions within presolar graphite grains (14), raising the prospect that SiC acts as a protective coating (against acid attack) for ultrarefractory metal condensates. Graphite is soluble in nitric acid, and Os alloys are expected to dissolve in aqua regia, so these grains are not the likely carriers of the observed anomaly given that such grains would have been consumed in the digestions carried out here, unless shielded in a resistant phase such as SiC.

Chondrite metamorphism has been documented to destroy presolar graphite and SiC (18). SiC typically has not survived to higher metamorphic grades of  $>3.8$  for ordinary chondrites, and  $\sim 5$  for enstatite chondrites (19, 20) consistent with such samples showing no Os isotope anomalies (Fig. 2). Thus, the likely interpretation is that an undigested carrier phase, probably SiC, retains the presolar  $s$ -process Os required to yield the solar  $s/r$  ratio for Os exhibited by H-group ordinary chondrites and terrestrial samples (Fig. 2). This is supported by the observation that two chondrites that underwent less metamorphism—Parnallee (LL3.6) and Indarch (EH4)—show  $s$ -process anomalies in their Os isotope profiles, but less so than Tagish Lake (C2) and Ornans (CO3). Presolar SiC is present in Indarch and some unequilibrated ordinary chondrites (19, 20). Sharps (H3.4) and Chainpur (LL3.6) do not exhibit Os isotope anomalies but instead plot within the range of epsilon values exhibited by the other H-group ordinary chondrites in Fig. 2.

Although most of Os originates in the  $r$  process (90%), about 10% of the solar system Os is produced by the  $s$  process (6–8). Correlated trends between  $\epsilon_{186}^{186}\text{Os}$ ,  $\epsilon_{188}^{188}\text{Os}$ , and  $\epsilon_{190}^{190}\text{Os}$  can be used to evaluate the nature of the anomalous Os isotopic component (Fig. 3). Mixing lines between average  $s$ -process Os isotopic composition (8) and average solar Os (i.e.,  $\epsilon_{186}^{186}\text{Os}$ ,  $\epsilon_{188}^{188}\text{Os}$ , and  $\epsilon_{190}^{190}\text{Os} = 0$ ) are resolvable from the correlations of the chondrite data for  $\epsilon_{188}^{188}\text{Os}$  to  $\epsilon_{186}^{186}\text{Os}$  and  $\epsilon_{190}^{190}\text{Os}$  to  $\epsilon_{186}^{186}\text{Os}$  but match the  $\epsilon_{188}^{188}\text{Os}$  to  $\epsilon_{190}^{190}\text{Os}$  correlation within error of the measurements (Fig. 3). This implies that the  $^{186}\text{Os}/^{188}\text{Os}$  ratio of the anomalous  $s$ -process component was lower relative to average solar system  $s$ -process Os. Here, we term this insoluble Os component Os(i). There are two branches in the  $s$ -process pathway at  $^{185}\text{W}$  and  $^{186}\text{Re}$  that allow the  $s$  process to flow to  $^{186}\text{W}$ ,  $^{187}\text{Re}$ , and then to  $^{188}\text{Os}$  (Fig. 1). Neutron capture on  $^{185}\text{Re}$  forms  $^{186}\text{Re}$  that decays 92% of the time by  $\beta^-$  (half-life of 3.8 days) to  $^{186}\text{Os}$ . The two branch points are relatively insensitive to stellar temperature but sensitive to stellar neutron density. These branch points have been used to estimate that the neutron density for average solar  $s$  process is  $4 \times 10^8$  n/cm<sup>3</sup> (5, 21). The Os(i) fraction of the solar  $s$  process requires a stellar source with higher

neutron density. The neutron density ( $n_n$ ) of the source was modeled by solving the simultaneous linear equations describing  $s$ -process flow with  $\beta^-$  decay branching to yield

$$\frac{\langle\sigma\rangle N_s)_{186\text{Os}}}{\langle\sigma\rangle N_s)_{188\text{Os}}} = \left(\frac{\lambda_{\beta^-}}{\lambda_{\beta^-} + v_T n_n \langle\sigma\rangle}\right)_{185\text{W}} \times \left(\frac{\lambda_{\beta^-}}{\lambda_{\beta^-} + v_T n_n \langle\sigma\rangle}\right)_{186\text{Re}} \times \prod_{A=185}^{A=188} \left[1 + \frac{1}{\tau_0 \langle\sigma\rangle_{A_i}}\right] \quad (1)$$

where  $v_T$  is the thermal neutron velocity,  $\lambda$  is the decay constant,  $N_s$  is the  $s$ -process abundance,  $\langle\sigma\rangle$  is the Maxwellian-averaged neutron capture cross-section, and  $\tau_0$  is the average neutron exposure (21). The branching decay of  $^{186}\text{Re}$  to  $^{186}\text{W}$  by electron capture was neglected for this calculation, because electron capture is diminished at the higher degree of ionization prevailing in stellar interiors (22). Using cross-sections, decay constants, and  $\tau_0$  typical of the  $s$  process (5, 21, 22), we calculated  $^{186}\text{Os}/^{188}\text{Os}$  ratios as a function of stellar neutron density and temperature (Fig. 4). The calculated neutron density for solar  $s$  process is similar to that obtained in (21). The  $^{186}\text{Os}/^{188}\text{Os} \sim 0.48$  in Tagish Lake Os(i) is matched at stellar neutron densities of  $6 \times 10^8$  to  $10 \times 10^8$  n/cm<sup>3</sup>.

There are two major neutron sources for the  $s$  process produced by helium-burning stellar reactions ( $\alpha$  capture):  $^{13}\text{C}(\alpha, n)^{16}\text{O}$  and  $^{22}\text{Ne}(\alpha, n)^{25}\text{Mg}$ . The  $^{13}\text{C}$ -source operates at  $T \sim 1 \times 10^8$  K and the  $^{22}\text{Ne}$  source operates at  $T \sim 3 \times 10^8$  K (8, 23). Coupled models of stellar evolution and nucleosynthesis in low-mass asymptotic giant branch stars indicate that during a double neutron pulse the  $^{22}\text{Ne}$  source contributes importantly to the abundances of nuclides produced at high neutron densities (up to  $10^{10}$  n/cm<sup>3</sup>) (23). This has been identified with the meteoritic Ne-E(H) component (23) and may also contribute the Os(i) component in Tagish Lake. Likely, the main component of  $s$ -process Os (and other heavy elements) may be resolved to be a mixture of varied neutron density sources operating in multiple low-mass stars with variable metallicity. Our technique resolved solar  $s$ -process Os in primitive chondrites into two components: Os(i) that is likely trapped in SiC grains, and aqua regia-soluble Os that is hosted by other phases (magnetite or Fe sulfides), which provide insights into the galactic chemical evolution of Os. The extractable Os either condensed into acid-soluble minerals from stellar outflows with  $\text{C/O} < 1$ , or it initially condensed in SiC grains which were then selectively destroyed in the interstellar medium (possibly older grains).

This interpretation—that the anomalous Os isotopic composition in unequilibrated

chondrites results from incomplete access of up to 50 ppm of the total Os present during digestion—has important ramifications to understanding the presence or absence of isotopic anomalies in bulk meteorites for other elements, including Zr, Mo, and Ru (4, 24–29). Because the Os abundance in bulk meteorites is small ( $\leq 1$  ppm) and because Os is one of the first elements to condense, mixing within the solar nebula before condensation into planetesimals must have been extremely efficient in order to result in a homogeneous Os isotopic composition of  $\pm 0.25$  epsilon units (i.e.,  $\pm 25$  ppm) observed in chondrites with greater metamorphic equilibration.

References and Notes

1. E. Zinner, *Annu. Rev. Earth Planet Sci.* **26**, 147 (1998).
2. L. R. Nittler, *Earth Planet. Sci. Lett.* **209**, 259 (2003).
3. M. T. McCulloch, G. J. Wasserburg, *Astrophys. J.* **220**, L15 (1978).
4. Q. Yin, S. Jacobsen, K. Yamashita, *Nature* **415**, 881 (2002).
5. F. Käppeler, R. Gallino, M. Busso, G. Picchio, C. M. Raiteri, *Astrophys. J.* **354**, 630 (1990).
6. E. Anders, N. Grevesse, *Geochim. Cosmochim. Acta* **53**, 197 (1989).
7. H. Palme, H. Beer, *Landolt-Bornstein New Series VI/3a* (Springer-Verlag, Berlin, 1993), pp. 196–221.
8. H. Beer, F. Corvi, P. Mutti, *Astrophys. J.* **474**, 843 (1997).
9. Materials and methods are available as supporting material on Science Online.
10. The traditional normalization to  $^{188}\text{Os}$  results in the same systematic differences between the chondrites, but the patterns are shifted and  $s$ -process anomalies are obscured because of the relative deficiency of  $^{188}\text{Os}$  due to  $s$  process.
11. I. Leya, R. Wieler, A. N. Halliday, *Geochim. Cosmochim. Acta* **67**, 529 (2003).
12. T. Nakamura, T. Noguchi, M. E. Zolensky, N. Takaoka, *Lunar Planet. Sci.* XXXII, 1621 (abstr.) (2001).
13. R. J. Walker et al., *Geochim. Cosmochim. Acta* **66**, 4187 (2002).
14. T. K. Croat, F. J. Stadermann, T. J. Bernatowicz, *Lunar Planet. Sci.* XXXVI, 1507 (abstr.) (2005).

15. Y. Kashiv, Z. Cai, B. Lai, S. R. Sutton, R. S. Lewis, A. M. Davis, R. N. Clayton, M. J. Pellin, *Lunar Planet. Sci.* XXXII, 2192 (abstr.) (2001).
16. H. Becker et al., *Lunar Planet. Sci.* XXXV, 1310 (abstr.) (2004).
17. M. M. Grady, A. B. Verchovsky, I. A. Franchi, I. P. Wright, C. T. Pillinger, *Meteorit. Planet. Sci.* **37**, 713 (2002).
18. G. R. Huss, *Nature* **347**, 159 (1990).
19. G. R. Huss, R. S. Lewis, *Geochim. Cosmochim. Acta* **59**, 115 (1995).
20. G. R. Huss, in *Astrophysical Implications of the Laboratory Study of Presolar Materials*, T. J. Bernatowicz, E. Zinner, Eds. (Proceedings of the American Institute of Physics, New York, 1997), vol. 402, pp. 721–748.
21. F. Käppeler, S. Jaag, Z. Y. Bao, G. Reffo, *Astrophys. J.* **366**, 605 (1991).
22. K. Takahashi, K. Yokoi, *Atomic Data Nucl. Data Tables* **36**, 375 (1985).
23. R. Gallino et al., *Astrophys. J.* **497**, 388 (1998).
24. N. Dauphas, B. Marty, L. Reisberg, *Astrophys. J.* **565**, 640 (2002).
25. J. H. Chen, D. A. Papanastassiou, G. J. Wasserburg, H. H. Ngo, *Lunar Planet. Sci.* XXXV, 1431 (abstr.) (2004).
26. D. A. Papanastassiou, J. H. Chen, G. J. Wasserburg, *Lunar Planet. Sci.* XXXV, 1828 (abstr.) (2004).
27. H. Becker, R. J. Walker, *Nature* **425**, 152 (2003).
28. H. Becker, R. J. Walker, *Chem. Geol.* **196**, 43 (2003).
29. M. Schönbächler et al., *Earth Planet. Sci. Lett.* **216**, 467 (2003).
30. We thank the NASA Cosmochemistry program for funding NAG5-13133 (M.H.), NNG05GB81G (M.H.), and RTOP 344-31-72-06 (A.B.). Samples were obtained from the Field Museum of Natural History, American Museum of Natural History, Museum National d'Histoire Naturelle, Natural History Museum of London, and the Smithsonian Institution. We thank H. Becker and an anonymous reviewer for journal reviews.

Supporting Online Material

www.sciencemag.org/cgi/content/full/309/5738/1233/DC1  
Materials and Methods  
Figs. S1 and S2  
Tables S1 to S4  
References

19 May 2005; accepted 20 July 2005  
10.1126/science.1115053

# The Illusion of Invariant Quantities in Life Histories

Sean Nee,<sup>1\*</sup> Nick Colegrave,<sup>1</sup> Stuart A. West,<sup>1</sup> Alan Grafen<sup>2</sup>

Life-history theory attempts to provide evolutionary explanations for variations in the ways in which animal species live their lives. Recent analyses have suggested that the dimensionless ratios of several key life-history parameters are the same for different species, even across distant taxa. However, we show here that previous analyses may have given a false picture and created an illusion of invariants, which do not necessarily exist; essentially, this is because life-history variables have been regressed against themselves. The following question arises from our analysis: How do we identify an invariant?

Key parameters that determine how species live their lives are the size at which weaning and sexual maturity occur, the number of offspring produced per year, and life span, among others (1–3). A recent approach to understanding the evolution of such life-history parameters has been to show how these analyses can be simplified by examining dimensionless ratios of these parameters, such

as the ratio of offspring weaning weight to maternal weight (1). This approach has been stimulated by analyses that suggest that these dimensionless ratios can be the same for different species, within and even across taxa (Table 1) (1, 4–13). These life-history invariants can be extremely striking, with the regression analyses used to test for them usually explaining 70 to 97% of the variation

## Analytical Techniques

Chondrite samples were measured for highly siderophile element concentrations (Ru, Pd, Re, Os, Ir, and Pt) and precise Os isotopic composition using previously established techniques (1). These data are listed in Tables S1, S2, and S3. Between 0.1 and 0.3 g of bulk sample powder and 5 mL of inverse *aqua regia* were placed into borosilicate glass Carius tubes and chilled to 0°C. The tubes were then sealed and heated in an oven to 270°C for ~72 hours. One Tagish Lake sample (MCO1, Hi T,P, Tables S1, S2), was digested at 325°C for 1 week in a sealed metal jacket pressurized with CO<sub>2</sub>. For some of the samples where precise Re and PGE data were not available (Table S3), after the tubes were opened, 5% of the sample solution from each of the Carius tubes was transferred into a new Carius tube for precise determination of the Pt/Os ratio. Before the transfer procedure, the Carius tube was chilled to 0°C and an appropriate amount of a mixed Re-PGE spike (#000601) was added to it, followed by inverse *aqua regia* after the sample solution transfer was completed. This new tube was then sealed and kept in an oven at ~250°C for 24 hours to achieve sample-spike equilibration. After opening the tube, the spiked aliquot was processed for Re and PGE, mainly to obtain the Pt/Os ratio for correcting <sup>186</sup>Os/<sup>188</sup>Os to initial at 4.558 Ga. From the remaining 95% of the unspiked *aqua regia* sample solution, Os was extracted into CCl<sub>4</sub>, and then back-extracted into HBr, followed by purification via microdistillation. The clean Os cuts from each of the unspiked Carius tube digestions were used for the precise measurements of the Os isotopic composition.

The high-precision measurements of the Os isotopic compositions were performed by N-TIMS in static mode on an eight-Faraday collector ThermoFinnigan Triton® mass spectrometer at the Johnson Space Center. The virtual amplifier system, that seeks to eliminate amplifier calibration bias, was used to increase reproducibility of the measured ratios. Signals of 150-250 mV on mass 234 (<sup>186</sup>Os<sup>16</sup>O<sub>3</sub><sup>-</sup>) and 235 (<sup>187</sup>Os<sup>16</sup>O<sub>3</sub><sup>-</sup>), and corresponding voltages of up to 6V for the Os isotopes with greater atomic abundance (e.g. <sup>188</sup>Os, <sup>189</sup>Os, <sup>190</sup>Os, <sup>192</sup>Os) were generated for ≥180 ratios to reach the desired run precision of ±15 ppm or better (2σ mean) for the <sup>186</sup>Os/<sup>188</sup>Os ratio, with corresponding run precisions for <sup>187</sup>Os/<sup>188</sup>Os, <sup>189</sup>Os/<sup>188</sup>Os, <sup>190</sup>Os/<sup>188</sup>Os. Each sample load was run one to six times.

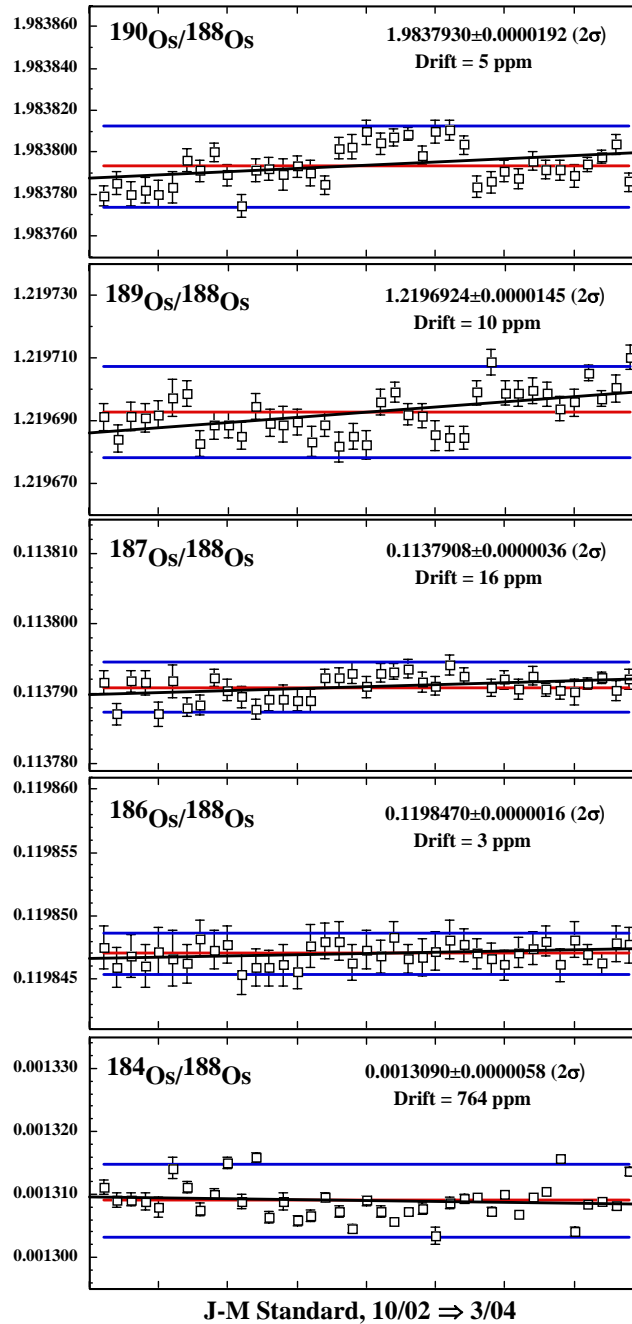
Measurements of Os, Ir, Ru, Pt, Pd, and Re isotopic compositions were performed on a ThermoFinnigan Element™ single-collector, magnetic sector ICPMS at The University of Chicago. The sample solutions were introduced into the ICPMS torch via a CETAC MCN6000

desolvating nebulizer for the PGE measurements or an ESI™ low-flow nebulizer for the Re measurements. Typical count rates were  $10^5$ - $10^6$  cps for PGEs and  $10^4$ - $10^5$  cps for Re, and the internal precisions of individual runs were better than 0.5% relative ( $2\sigma$  mean). Long-term reproducibilities of 0.5 ppb in-house Ir-Ru-Pd-Pt and Re standard solutions and a 1 ppb Os standard solution, which characterize the external precision of the analysis, were 1-2% ( $2\sigma$  stdev) on all isotope ratios. Mass fractionation for Ru, Pd, Ir, Pt, and Re was corrected using  $^{99}\text{Ru}/^{102}\text{Ru} = 0.4044$ ,  $^{110}\text{Pd}/^{106}\text{Pd} = 0.4288$ ,  $^{191}\text{Ir}/^{193}\text{Ir} = 0.5942$ ,  $^{198}\text{Pt}/^{195}\text{Pt} = 0.2130$ , and  $^{185}\text{Re}/^{187}\text{Re} = 0.5974$  relative to those measured in the standard solutions that were run alternately with the samples. The measured  $^{190}\text{Os}/^{192}\text{Os}$  ratios in the samples were corrected for fractionation using a linear law and  $^{192}\text{Os}/^{188}\text{Os} = 3.083$ . The average total analytical blank was 5 pg Os, 0.5 pg Ir, 3 pg Ru, 31 pg Pt, 7 pg Pd, and 10 pg Re. Blank corrections applied were <0.1%.

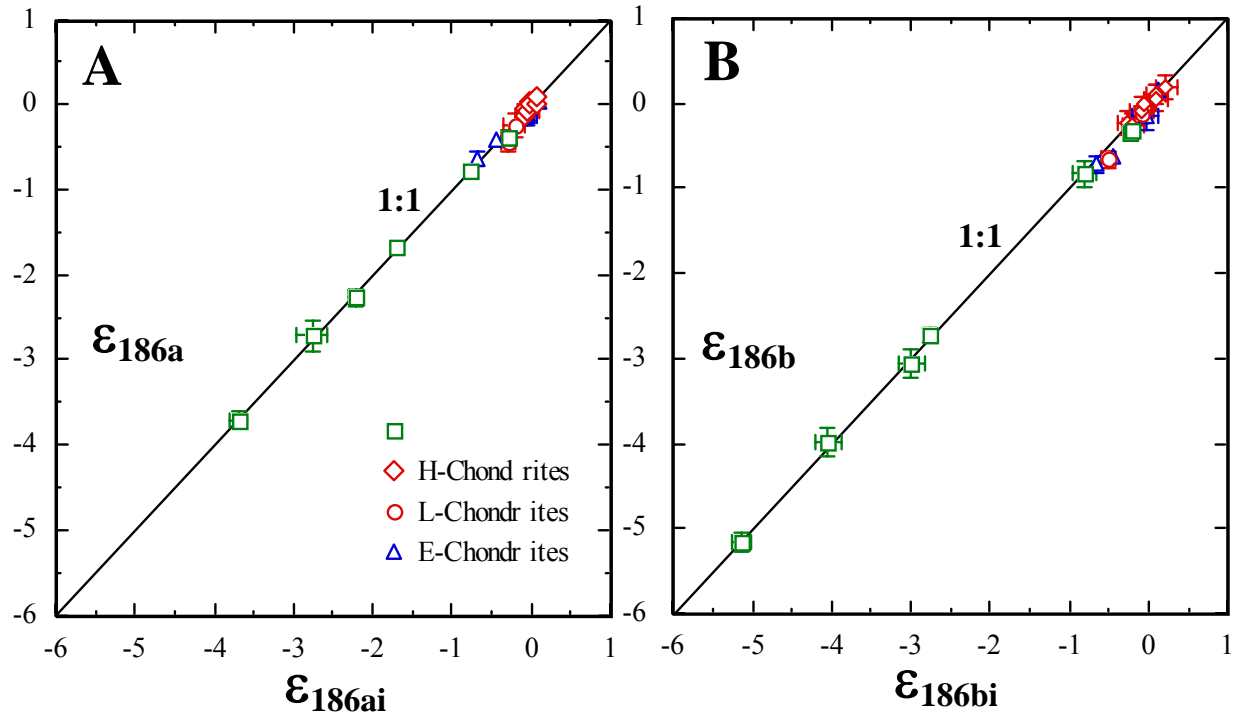
### **Mass Fractionation Corrections, Data Handling, Interferences.**

Table S2 reports the measured isotope ratios normalized to the isotope of  $^{188}\text{Os}$  and corrected for instrumental mass fractionation using  $^{192}\text{Os}/^{188}\text{Os} = 3.083$  and the exponential law. Data for 39 runs of the Johnson-Matthey Os standard during the analytical campaign are presented in Table S2. Figure S1 shows the standard data for each isotope ratio plotted in sequence over time, measured during the analytical campaign over an approximately 1.5 year period. The average for each ratio and the external precision ( $\pm 2\sigma$  mean) are plotted and listed. A regression line through each sequence shows that while it may be possible that a drift occurred over time, this drift for each ratio, if present, is well within the  $\pm 2\sigma$  external precisions. Hence no second order corrections were applied to the data presented in Tables S1 and S2. The data are reported in the epsilon notation where  $\epsilon_{\text{Os}}$  (e.g.  $\epsilon_{184a}$ , etc.) is  $10^4$  parts deviation from a standard value, in this case, bulk solar values based on the averages of H-Group ordinary chondrites. See the text in the paper for justification of this approach. Note that the averaged epsilon values for the replicate measurements of the Johnson-Matthey terrestrial standard values listed in Table S2, overlap within measured uncertainty, with the defined solar values with the exception of  $^{186}\text{Os}/^{188}\text{Os}$ . This is because the present day measured standard has a radiogenic  $^{186}\text{Os}/^{188}\text{Os}$  as a result of superchondritic  $^{190}\text{Pt}/^{188}\text{Os}$  and subsequent in growth of  $^{186}\text{Os}$  over time, and hence is not applicable to this study with the exception of defining external precision. Note that because

$^{188}\text{Os}$  and  $^{192}\text{Os}$  are used as normalizing isotopes, their respective  $\epsilon_{188a}$  and  $\epsilon_{192a}$  values for all samples are zero. For the measured  $\epsilon_{186a}$  and initial  $^{186}\text{Os}/^{188}\text{Os}$  isotopic compositions at 4.558 Ga ( $\epsilon_{186ai}$  in Table S2, Figure S2A), the average of H-Group ordinary chondrites from this study were used as the normalizing ratios to determine deviations from these samples.



**Figure S1.** Oxygen and fractionation corrected (using  $^{192}\text{Os}/^{188}\text{Os} = 3.083$ ) ratios measured for the Johnson-Matthey Os standard over the time of this study.



**Figure S2.** A. The measured  $^{186}\text{Os}/^{188}\text{Os}$  (shown as  $\epsilon_{186a}$  values), versus calculated values ( $\epsilon_{186ai}$ ) at 4.558 Ga, using  $^{190}\text{Pt}/^{188}\text{Os}$  ratios in Table S3. Error bars are  $2\sigma$ . B. The measured  $^{186}\text{Os}/^{189}\text{Os}$  (shown as  $\epsilon_{186b}$  values), versus calculated values ( $\epsilon_{186bi}$ ) at 4.558 Ga, using  $^{190}\text{Pt}/^{189}\text{Os}$  ratios converted from  $^{190}\text{Pt}/^{188}\text{Os}$  in Table S3. Error bars are  $2\sigma$ .

The average present-day  $^{186}\text{Os}/^{188}\text{Os}$  of the H-Group chondrites in Table S2 is  $0.1198398 \pm 7$  ( $n=5$ ), while the average initial  $^{186}\text{Os}/^{188}\text{Os}$  is  $0.1198270 \pm 8$ , using the Pt/Os ratios in Table S3 to correct for  $^{186}\text{Os}$  production from the decay of  $^{190}\text{Pt}$  over the solar system history. The  $\epsilon_{186ai}$  values for all chondrites in Table 2S were corrected for  $^{190}\text{Pt}$  decay to initial using Pt/Os ratios in Table S3. The Pt/Os ratios in these chondrites vary from 1.71 to 2.09, overlapping the range of a comprehensive suite of chondrites (2). Given the long half-life of the parent isotope  $^{190}\text{Pt}$  of 469 Ga ( $\lambda = 1.477 \times 10^{-12}$  [3]), in combination with this restricted range in Pt/Os for chondrites, and the minor abundance of  $^{190}\text{Pt}$  (0.01292 atomic%), results in a systematic correction of all  $^{186}\text{Os}/^{188}\text{Os}$  measured data to initial of  $107 \pm 10$  ppm and error propagation from this correction to initial is  $\leq 5$  ppm in each sample, and does not affect the systematics  $^{186}\text{Os}$  observed in Table S2 (Figure S2A). This is because of the long half-life of

$^{190}\text{Pt}$  and the small range of the Pt/Os ratios of all samples results in an internal variability by the correction (how much the corrections differ for various samples) that is much smaller than the total correction.

The observed isotopic variations between the chondrites, the terrestrial standard, and terrestrial samples listed in Table S2, indicate that some chondrites are either deficient in  $^{188}\text{Os}$  or enriched in  $^{189}\text{Os}$  in comparison to the terrestrial samples. For example, measurements for Tagish Lake aliquots show elevated  $^{189}\text{Os}/^{188}\text{Os}$  relative to the terrestrial standard, terrestrial samples, Allende, ordinary, and enstatite chondrites. If these elevated  $^{189}\text{Os}/^{188}\text{Os}$  values are a result of depletion in  $^{188}\text{Os}$ , then using  $^{188}\text{Os}$  as a normalizing isotope results in deviation from the true epsilon values for each isotope. The magnitude of the deviation of the epsilon values from their true values is dependent on the magnitude of deviation of  $^{188}\text{Os}$  abundance from the standard value. Ideally, the optimal approach is to use two isotopes with either no or the smallest natural variance to correct for mass fractionation and to use as a normalizing isotope. As this work shows, we have reason to believe that  $^{188}\text{Os}$  may be deficient in some of the chondrites as a result of a missing s-process carrier, which would have minimal effect on  $^{189}\text{Os}$ . The  $^{189}\text{Os}$  and  $^{192}\text{Os}$  isotopes were used because they are composed approximately 4.8% and 0% of s-process component for bulk solar Os, respectively, and hence, variations reflecting the presence or absence of an s-process component are most easily illustrated in this fashion. Hence in Tables S1 and S2, the epsilon values normalized to  $^{189}\text{Os}$  are also presented. The raw data from the runs are normalized to  $^{189}\text{Os}$  and corrected for instrumental mass fractionation using the exponential law where  $^{192}\text{Os}/^{189}\text{Os} = 2.5276865$ , which is based on  $^{192}\text{Os}/^{188}\text{Os} = 3.083$  (1,4), and the measured  $^{189}\text{Os}/^{188}\text{Os}$  of 1.2196924 for the standard (Table S2, Figure S1). Because  $^{189}\text{Os}$  and  $^{192}\text{Os}$  are used for normalizing the raw data, all data have  $\epsilon_{189\text{Osb}}$  and  $\epsilon_{192\text{Osb}}$  of 0 in these calculations. The initial  $^{186}\text{Os}/^{189}\text{Os} = 0.0982427$  used to calculate initial epsilon values ( $\epsilon_{186\text{Obi}}$ ) is equivalent to  $^{186}\text{Os}/^{188}\text{Os} = 0.1198270$ , based on the average of the ordinary chondrite data corrected to initial from the raw data in this method and the Pt/Os ratios listed in Table S3. This results in a systematic correction of all  $^{186}\text{Os}/^{189}\text{Os}$  measured data to initial ( $\epsilon_{186\text{Obi}}$ ) of approximately  $107 \pm 10$  ppm with an error propagation from this correction to initial is  $\leq 5$  ppm in each sample, and does not affect the systematics  $^{186}\text{Os}$  observed in Tables S1 and S2 (Figure S2B). This correction is identical to that applied to  $^{186}\text{Os}$  when normalized to  $^{188}\text{Os}$  as discussed above.

Note that epsilon values for  $^{184}\text{Os}$  and  $^{187}\text{Os}$  that are calculated from the  $^{192}\text{Os}/^{189}\text{Os}$  normalization are not reported in Table S1 and S2. The isotope  $^{184}\text{Os}$  is a 100% p-process isotope. Because of its minor abundance ( $\sim 0.02$  atomic%), precise measurement of this isotope at the epsilon level is not possible under the conditions that Os is run on the Triton. The  $2\sigma$  uncertainty for 39 runs of the Johnson Matthey standard for  $^{184}\text{Os}/^{188}\text{Os}$  was  $\pm 44$  epsilon units (Table S2). All of the sample data plot within this external precision. The isotope  $^{187}\text{Os}$  poses another problem. As in the case for  $^{186}\text{Os}$ ,  $^{187}\text{Os}$  is a 100% s-process isotope for initial solar composition. However, like  $^{186}\text{Os}$ ,  $^{187}\text{Os}$  is also in part radiogenic as a decay from  $^{187}\text{Re}$  when measuring present-day samples, and a correction must be made. Unlike the special circumstances discussed above that results in relatively minor and systematic correction to initial for  $^{186}\text{Os}$ , the correction to initial for  $^{187}\text{Os}$  is complicated by a  $\sim 10$  times shorter half-life (41.6 Ga) and  $\sim 3000$  times greater abundance (37.4 atomic%) of  $^{187}\text{Re}$  when compared to  $^{190}\text{Pt}$ . Hence the increase in  $^{187}\text{Os}$  over solar system history in chondrites has ranged from 25 to 38% due to variation in the Re/Os of each sample (compared to  $\sim 110$  ppm for  $^{186}\text{Os}$ ), producing large error propagations of at least at the per mil level (1 per mil is 10 epsilon units). This renders the initial  $^{187}\text{Os}$  unusable for detecting isotope anomalies at the  $< 5$ -epsilon unit level.

One possible mechanism to develop some of the isotope anomalies observed is by unrecognized mass interferences. In order to determine if interferences were present, mass scans were performed on the Os Johnson-Matthey standard and Tagish Lake sample MC01 after completing a successful run, and still at operating conditions. Table S4 lists the observed masses and beam intensities across the mass spectrum of 0 to 252. Beam intensities for  $\text{Os}^{16}\text{O}_3^-$  isotopes during the scan with masses ranging from 232 to 240 were typical of run conditions for the data presented in Table S2. The table lists all masses with peak sizes of more than 50 counts per second on the electron multiplier. Given the beam intensities for the Os isotopes, an interference with 1000 counts per second would be 10 ppm on 1V, and 100 counts per second would be 6.7 ppm on 150 mV, the typical beam intensities for  $^{188}\text{Os}^{16}\text{O}_3^-$  and  $^{186}\text{Os}^{16}\text{O}_3^-$ , respectively, during run conditions. With the exception of 4 masses ranging from mass 60 to mass 76, all of the peaks were readily identified, and do not produce additional known complex oxides or other atoms that would interfere with masses from 232 to 240. All of the identified masses, consisting of oxygen, noble elements and their oxides, halogens, were present in both the standard and Tagish Lake MC01 runs, with one exception. In MC01,  $\text{Cr}^{16}\text{O}_3^-$  isotopes were present from

masses of 98 to 102 but are not present in the standard run. This is explained by the fact that chromium VI is used in sulfuric acid as an oxidant in the final microdistillation stage for Os purification. All samples processed in this way will thus have minor amounts of these  $\text{Cr}^{16}\text{O}_3^-$  masses, and this cannot account for any interferences that could create the Os isotopic distinctions for the Tagish Lake and other samples relative to each other. Of significant importance, no evidence of any organic material, besides very small peaks at  $^{12}\text{C}$ , were found in either the standard or the MC01 mass spectrum (Table S4). Hence, it can be concluded that for our best possible means of evaluation, no interferences are present that can cause any significant shifts in the Os isotopic compositions in the mass range of 232 to 240 where the  $\text{Os}^{16}\text{O}_3^-$  are measured.

## References

- (1) I.S. Puchtel, A.D. Brandon, M. Humayun, *Earth Planet. Sci. Lett.* 224, 157 (2004).
- (2) M.F. Horan, R.J. Walker, J.M. Morgan, J.N. Grossman, and A.E. Rubin, *Chem. Geol.* 193, 5 (2003).
- (3) D.L. Cook, R.J. Walker, M.F. Horan, J.T. Wasson, J.W. Morgan, *Geochim. Cosmochim. Acta* 68, 1413 (2004).
- (4) A.D. Brandon, R.J. Walker, I.S. Puchtel, H. Becker, M. Humayun, S. Revillon, *Earth Planet. Sci. Lett.* 206, 411 (2003).
- (5) R.J. Walker, A.D. Brandon, J.M. Bird, P.M. Piccoli, W.F. McDonough, R.A. Ash, *Earth Planet. Sci. Lett.* 230, 211 (2005).
- (6) A.D. Brandon, M. Humayun, I.S. Puchtel, *Geochim. Cosmochim. Acta* 69, 1619 (2005).

**Table S1.** Epsilon values for Os isotopes in chondrites, a terrestrial standard, and terrestrial Os-rich alloys, where  $\varepsilon = 10^4$  deviation from the averages of H-Group ordinary chondrites. The  $\varepsilon_{186i}$  values are for initial  $\varepsilon_{186}$  ( $^{186}\text{Os}$  corrected for  $^{190}\text{Pt}$  decay over 4.558Ga to present). The  $^{192}\text{Os}/^{189}\text{Os}$  ratio was used to correct for instrumental mass fractionation. See Supporting Online Material for additional data and discussion.

Sample (Group)	$\varepsilon_{186}$	$\varepsilon_{186i}$	$\pm 2\sigma$	$\varepsilon_{188}$	$\pm 2\sigma$	$\varepsilon_{190}$	$\pm 2\sigma$
Allende Fraction 1 (CV3)	-0.33	-0.23	0.05	0.05	0.02	0.07	0.01
Allende Fraction 2	-0.31	-0.21	0.09	0.04	0.03	-0.02	0.02
Tagish Lake KN2 (C2)	-3.05	-2.99	0.17	-0.57	0.07	-0.38	0.05
Tagish Lake MC01	-3.99	-4.04	0.17	-0.84	0.07	-0.46	0.01
Tagish Lake MC01,HiT,P	-2.72	-2.76	0.09	-0.71	0.06	-0.45	0.03
Tagish Lake MH11	-5.16	-5.15	0.12	-0.98	0.01	-0.62	0.08
Ornans (CO3)	-0.83	-0.81	0.15	-0.04	0.04	-0.03	0.03
Sharps Fraction 1 (H3.4)	0.06	0.10	0.15	0.10	0.05	0.07	0.05
Sharps Fraction 2	-0.25	-0.20	0.13	-0.14	0.05	-0.11	0.03
St. Marguerite (H4)	-0.22	-0.26	0.14	-0.12	0.04	-0.05	0.08
St. Marguerite Metal	0.00	-0.05	0.08	-0.01	0.03	-0.03	0.03
Forest Vale (H4)	0.18	0.22	0.14	0.12	0.05	0.04	0.03
Weston (H5)	0.10	0.08	0.12	0.02	0.04	0.02	0.01
Allegan (H5)	-0.08	-0.09	0.15	-0.05	0.07	-0.04	0.05
Avg. H Ordinary Chondrites (n=5)	0.00	0.00	0.15	0.00	0.07	0.00	0.03
Chainpur (LL3.4)	-0.13	-0.08	0.10	0.08	0.01	0.01	0.02
Parnellee (LL3.6)	-0.66	-0.51	0.10	-0.13	0.04	-0.09	0.07
Indarch Fraction 1 (EH4)	-0.72	-0.75	0.09	-0.05	0.04	-0.11	0.05
Indarch Fraction 2	-0.63	-0.66	0.08	-0.15	0.03	-0.13	0.02
Yilmia Fraction 1 (EL6)	-0.08	-0.10	0.08	0.01	0.03	-0.13	0.02
Yilmia Fraction 2	-0.16	-0.09	0.16	-0.02	0.05	-0.06	0.06
Daniels Kuil (EL6)	0.16	0.24	0.07	0.10	0.01	0.08	0.03
Terrestrial Standard (n=39)	0.67		0.25	0.06	0.16	-0.01	0.14
Lamellae 1-4	0.00		0.03	0.01	0.03	-0.04	0.02
Lamellae 2-6	-0.23		0.08	-0.03	0.04	-0.10	0.04
Lamellae 5-3	-0.28		0.07	-0.04	0.01	-0.15	0.02
Marix 7-5	-0.36		0.17	-0.10	0.07	-0.14	0.06
Matrix 1-4	-0.01		0.15	0.03	0.07	-0.02	0.05

Matrix10-4	-0.33	0.04	-0.09	0.09	-0.13	0.03
------------	-------	------	-------	------	-------	------

Table S3. Rhenium and platinum group element concentrations for selected chondrites. Concentrations are in part per billion.

	wt. (gms)	Re	Os	Ir	Ru	Pt	Pd	Pt/Os	<sup>190</sup> Pt/ <sup>188</sup> Os	<sup>190</sup> Pt/ <sup>189</sup> Os
<b><u>Carbonaceous</u></b>										
Allende CV3 <sup>1</sup>	0.0523	63.5	784.9	720.4	1117.9	1421.5	681.7	1.811	0.001725	0.001414
<b><u>Tagish Lake C2</u></b>										
KN2 Fraction 1 <sup>1</sup>	0.0427	42.0	514.7	506.8	846.5	968.1	600.9	1.881	0.001791	0.001469
KN2 Fraction 2 <sup>1</sup>	0.0421	42.1	508.6	497.2	833.5	960.4	598.2	1.888	0.001798	0.001474
MC-01 <sup>1</sup>	0.0516	39.5	469.0	477.7	755.1	976.4	578.9	2.082	0.001983	0.001626
MH-11 <sup>1</sup>	0.0505	31.1	380.7	370.3	593.8	751.7	443.6	1.975	0.001881	0.001542
Carbonate-rich <sup>1</sup>	.0459	41.5	499.8	480.2	776.7	927.2	544.3	1.855	0.001767	0.001448
Ormans CO3	0.0147	54.9	680.6	691.6	1093.0	1336.2	779.8	1.963	0.001870	0.001533
<b><u>Ordinary</u></b>										
Sharps H3.4	0.0420	64.4	756.3	710.3	1149.3	1451.9	781.7	1.920	0.001829	0.001499
St.Marguerite H4										
Bulk	0.2564	64.7	712.6	642.1	1111.4	1477.4	808.4	2.073	0.001974	0.001619
Metal	0.1147	319.8	3149.3	2936.1	4989.8	6597.7	3818.6	2.095	0.001995	0.001636
Forest Vale H4 <sup>2</sup>	0.107	79.8	809.8	730.6	1141.0	1568.0	853.9	1.936	0.001844	0.001512
Weston H5	0.3099	77.8	827.7	795.3	1293.4	1685.9	922.0	2.037	0.001940	0.001591
Allegan H5	0.2942	76.0	760.9	719.5	1218.9	1544.5	882.4	2.030	0.001933	0.001585
Chainpur LL3.4 <sup>2</sup>	0.107	30.5	351.2	316.7	537.4	672.3	346.0	1.914	0.001823	0.001495
Parnallee LL3.6	0.6172	35.1	404.4	367.9	559.3	692.7	502.2	1.713	0.001631	0.001338
<b><u>Enstatite</u></b>										
Indarch EH4	0.146	46.6	520.0	512.3	847.3	1071.0	838.8	2.060	0.001962	0.001609
Yilmia EL6	0.133	60.3	937.0	886.7	1389.5	1749.4	1089.1	1.867	0.001778	0.001458
Daniels Kuil EL6 <sup>2</sup>	0.127	73.3	827.9	748.8	1168.0	1528.0	920.8	1.846	0.001758	0.001441

1 - Data from (6)

2 – Data from (2).

Table S4. Observed masses, negative ion mass scan from 0 to 252, for the Os standard and Tagish Lake MC01 following successful runs.

**red (bold) - SEM counts/second –  
100,000 counts = 0.001V**

If  $^{188}\text{OsO}_3 \geq 1\text{V}$ ,  
then 10 ppm = 1000 counts/sec, or 0.00001

*blue - Faraday voltages*

NO ; not observed

Mass 0-50	<u>12</u>	<u>16</u>	<u>26</u>	<u>27</u>	<u>32</u>	<u>35</u>	<u>37</u>	<u>42</u>	<u>43</u>			
Ion	$^{12}\text{C}$	$^{16}\text{O}$	$^{10}\text{B}^{16}\text{O}$	$^{11}\text{B}^{16}\text{O}$	$^{16}\text{O}_2$	$^{35}\text{Cl}$	$^{37}\text{Cl}$	$^{10}\text{B}^{16}\text{O}_2$	$^{11}\text{B}^{16}\text{O}_2$			
<b>Os std</b>	<b>250</b>	<b>130000</b>	<b>3500</b>	<b>14000</b>	<b>3800</b>	<i>1.28</i>	<i>0.41</i>	<i>0.30</i>	<i>1.1</i>			
<b>MC01</b>	<b>150</b>	<b>180000</b>	<b>NO</b>	<b>NO</b>	<b>5200</b>	<i>0.153</i>	<i>0.049</i>	<i>0.0055</i>	<i>0.020</i>			
Mass 50-150	<u>60</u>	<u>63</u>	<u>72</u>	<u>76</u>	<u>79</u>	<u>81</u>	<u>98</u>	<u>100</u>	<u>101</u>	<u>102</u>	<u>127</u>	
Ion					$^{79}\text{Br}$	$^{81}\text{Br}$	$^{50}\text{Cr}^{16}\text{O}_3$	$^{52}\text{Cr}^{16}\text{O}_3$	$^{53}\text{Cr}^{16}\text{O}_3$	$^{54}\text{Cr}^{16}\text{O}_3$	$^{127}\text{I}$	
<b>Os std</b>	<b>700</b>	<b>250</b>	<b>NO</b>	<b>350</b>	<i>&gt;0.05</i>	<i>&gt;0.05</i>	<b>NO</b>	<b>NO</b>	<b>NO</b>	<b>NO</b>	<b>70000</b>	
<b>MC01</b>	<b>3900</b>	<b>2800</b>	<b>1100</b>	<b>1900</b>	<i>&gt;0.05</i>	<i>&gt;0.05</i>	<i>0.00025</i>	<i>0.0046</i>	<i>0.0006</i>	<i>0.0002</i>	<b>5000</b>	
Mass 150-215	<u>192</u>	<u>194</u>	<u>195</u>	<u>196</u>	<u>197</u>	<u>198</u>	<u>208</u>	<u>210</u>	<u>211</u>	<u>212</u>	<u>214</u>	
Ion	$^{192}\text{Pt}$	$^{194}\text{Pt}$	$^{195}\text{Pt}$	$^{196}\text{Pt}$	$^{197}\text{Au}$	$^{198}\text{Pt}$	$^{192}\text{Pt}^{16}\text{O}$	$^{194}\text{Pt}^{16}\text{O}$	$^{195}\text{Pt}^{16}\text{O}$	$^{196}\text{Pt}^{16}\text{O}$	$^{198}\text{Pt}^{16}\text{O}$	
<b>Os std</b>	<b>&lt;100</b>	<b>&lt;1000</b>	<b>&lt;1000</b>	<b>&lt;1000</b>	<b>9000</b>	<b>&lt;1000</b>	<b>&lt;100</b>	<b>1000</b>	<b>1000</b>	<b>800</b>	<b>200</b>	
<b>MC01</b>	<b>800</b>	<b>35000</b>	<b>34000</b>	<b>25000</b>	<b>6000</b>	<b>6500</b>	<b>1000</b>	<b>42000</b>	<b>42000</b>	<b>29000</b>	<b>9000</b>	
Mass 215-255	<u>218-224</u>	<u>224-230</u>	<u>249,251</u>									
Ion	$\text{OsO}_2$	$\text{PtO}_3$	$\text{ReO}_4$									
<b>Os std</b>	<i>all peaks <math>\leq 0.007\text{ V}</math></i>											
<b>MC01</b>	<i>all peaks <math>\leq 0.005\text{ V}</math></i>											

**Operating conditions:**

**T = 850C, PO<sub>2</sub> = 2x10<sup>-7</sup> mbar.**